Fabrication Time Diagrams for In-Space Manufacturing of Large Reticulated Structures

Harsh G. Bhundiya
Department of Aeronautics and Astronautics,
Massachusetts Institute of Technology,
Cambridge, MA 02139

Michael A. Marshall
Space Exploration Sector,
The Johns Hopkins University
Applied Physics Laboratory,
Laurel, MD 20723

Zachary C. Cordero[1]
Department of Aeronautics and Astronautics,
Massachusetts Institute of Technology,
Cambridge, MA 02139
e-mail: zcordero@mit.edu

In-space manufacturing (ISM), or the construction of structures from raw feedstock materials in the space environment, is a promising approach for building large, external support structures for future space missions. Most research and development on ISM to date has focused on ground-based or microgravity-based demonstrations of candidate fabrication processes; however, the combined design of the ISM spacecraft and the fabrication process has not been fully investigated. In this paper, we estimate the fabrication times for truss support structures subject to various spacecraft constraints, including the available fabrication power, the attitude control system (ACS) authority, and the avoidance of control–structure interactions. Using the key assumptions of (1) a fabrication process that sequentially extrudes struts, (2) a fixed spacecraft orientation, and (3) negligible effects of environmental disturbance torques, we generate fabrication time diagrams that depict the dominant constraints and estimates of the fabrication time for a range of dimensions. Our results indicate that for large, dense reticulated geometries such as the curved gridshell and tetrahedral truss, the angular momentum storage of the spacecraft ACS is the dominant constraint on fabrication time. Additionally, our results suggest the following strategies for reducing fabrication time: manufacturing with multiple spacecraft; using stiff, lightweight feedstock; maximizing fabrication power and ACS capability; and minimizing spacecraft bus mass. These strategies represent design tradeoffs, emphasizing how the design of an ISM spacecraft cannot be considered independently of the fabricated structure.
[DOI: 10.1115/1.4066721]

Keywords: in-space manufacturing, truss structures, fabrication time, variable-mass rigid body dynamics, spacecraft systems engineering

1 Introduction

In-space manufacturing (ISM) refers to the construction of structures from raw feedstock materials in the space environment. Its key benefits include the fabrication of structures optimized for the space environment, increased mission flexibility through on-demand fabrication, and the potential to construct larger structures than those achievable with modern deployable technologies. A specific application of ISM that offers significant mass and cost savings [1] relative to current space mission architectures is large external structure manufacturing, which refers to the robotic fabrication of large support structures for payloads such as solar panels, radio frequency (RF) antennas, and space telescopes [2] whose performance increases with size. Recent models [3,4] suggest that ISM offers the largest cost savings relative to current space mission architectures by enabling the construction of large-diameter antennas in geostationary orbit.

Most research and development on ISM of large support structures has focused on ground-based or microgravity-based demonstrations of candidate fabrication processes. In the 1970s, for example, NASA developed and ground-tested two machines for fabricating truss beams on orbit, one which formed and spot-welded aluminum feedstock [5] and another which roll-formed and ultrasonically welded graphite fiber-reinforced plastic feedstock [6]. In 2007, NASA demonstrated an electron beam additive manufacturing process with metallic wire feedstock on a parabolic flight [7]. More recently, commercial companies such as Redwire Space and Tethers Unlimited have developed and vacuum-tested robotic systems for the extrusion of carbon fiber-reinforced plastic (CFRP) trusses [8,9]. Similarly, the company DCubed has developed a technique that uses UV photopolymer extrusion to fabricate lightweight truss structures; this technique has been flight-tested on a sounding rocket and is planned for a future spaceflight demonstration [10]. In parallel, we have developed a concept for forming truss structures via computer numerical control deformation processing of metallic feedstock, termed bend-forming, which has been demonstrated on the ground with 1-m prototypes [11]. This process relies on the extrusion of spooled feedstock with localized plastic deformation and mechanical joints at the nodes to form stiff, lightweight truss structures. Although each of these various candidate fabrication processes is envisioned to construct large truss structures, the combined design of the ISM spacecraft and the fabrication process has yet to be fully investigated. Understanding this relationship is crucial because the requirements of the fabrication process are coupled with those of the spacecraft.

---

[1]Corresponding author.
Manuscript received April 30, 2024; final manuscript received August 16, 2024; published online October 24, 2024. Assoc. Editor: Ajay P. Malshe.

Quantifying the fabrication time of support structures is particularly important for the design of future ISM spacecraft and missions. The fabrication time depends on various factors (e.g., the number of spacecraft and the complexity of the desired structure) but is ultimately constrained by spacecraft capabilities such as the available power and attitude control system (ACS) authority. Our previous analysis in Ref. [12] calculated feasible fabrication times of a tetrahedral truss via a spacecraft with a fixed power budget and a fabrication process with fixed specific energy consumption. However, it did not consider other constraints on fabrication time, particularly the ACS authority and the structural dynamics during fabrication. The unique challenges of attitude control during robotic fabrication [13] make these constraints important for the construction of large structures. In particular, active attitude control is critical during ISM due to the large changes in inertia properties of the spacecraft and the long time scales of fabrication. Additionally, the flexibility of the structure limits fabrication rates to avoid control–structure interactions and large amplitude vibrations during fabrication.

In this paper, we develop analytical and numerical frameworks to understand how spacecraft constraints on the available fabrication power, ACS authority, and flexible body dynamics affect the fabrication times for ISM of large, external support structures. We focus on the ISM of large truss structures via a fabrication process that sequentially extrudes struts and considers two efficient support structure geometries for reflector antennas and space telescopes, the curved gridshell and tetrahedral truss (Fig. 1) [2,14]. We summarize the insights in fabrication time diagrams which present the dominant constraints and estimates of total fabrication time for a wide range of dimensions. We then vary model parameters in case studies that explore the potential of these diagrams to aid feedstock material selection, fabrication process design, and ACS sizing for ISM spacecraft. Additionally, we discuss the implications of varying important assumptions in our analysis and conclude with recommendations for reducing the fabrication times of large truss structures.

2 Analysis

The total fabrication time for ISM of truss structures depends on many mission parameters, including the number of spacecraft, the capabilities of each spacecraft, the details of the fabrication process, and the geometry of the desired structures. To simplify the problem of estimating fabrication times, we consider an idealized spacecraft that constructs large reticulated geometries by sequentially extruding struts following a specified fabrication path. To model fabrication with multiple spacecraft, we assume that each spacecraft simultaneously fabricates an equal fraction of the total number of struts. We then estimate the total fabrication

Fig. 1 Support structures considered in this paper: curved gridshell and tetrahedral truss. Each geometry is parameterized by its diameter D and average strut length L.

time as the sum of the fabrication times for each strut, which is limited by four constraints:

- Maximum fabrication power, P_{max}
- Maximum ACS torque, τ_{max}
- Maximum ACS angular momentum storage, h_{max}
- Flexible body dynamics

The first constraint refers to the maximum power (P_{max}) a spacecraft can provide to its fabrication process. The electrical power system dictates this maximum power and limits the extrusion rate for processes with fixed specific energy consumption, i.e., the required energy per unit mass of feedstock material (u). For instance, melt-based processes like fused filament fabrication typically have a specific energy consumption of $u \approx 5\,\mathrm{MJ/kg}$ for most feedstock materials, whereas deformation processes have a lower specific energy consumption of $u \approx 0.5\,\mathrm{MJ/kg}$ for metals [12]. Assuming each strut is fabricated sequentially, a spacecraft with fixed power therefore limits the total fabrication time.

The second and third constraints relate to the ACS capabilities of the spacecraft. For ISM of large structures, active attitude control may be needed during fabrication to maintain the orientation of spacecraft subsystems such as solar panels and antennas despite large changes in inertia properties of the spacecraft and the long time scales of fabrication. Here, we assume that the spacecraft uses momentum actuators to maintain an inertially fixed orientation during the fabrication process. Consequently, the maximum available control torque (τ_{max}) and angular momentum storage (h_{max}) of these actuators limit the rate of each extrusion step. In practice, a fixed orientation may not be necessary during the entire fabrication process; however, this assumption allows for the derivation of simple relationships between the ACS authority and the fabrication time. We discuss the implications of relaxing this assumption on fabrication time in Sec. 5.

The final constraint applies a safety factor (SF) to the fabricated structure's fundamental natural frequency as a safeguard against unwanted control–structure interactions and the excitation of large amplitude structural vibrations. To avoid control–structure interaction, a standard practice is to place the closed-loop ACS bandwidth at least an order of magnitude below the fundamental natural frequency of the spacecraft [15]. By doing so, it is often possible to neglect structural flexibility and design the ACS as if the spacecraft is a rigid body. Similarly, extrusion-based ISM processes cause the fabricated structure to undergo large rigid body motions relative to the fabricating spacecraft. These rigid body motions are analogous to slew maneuvers, and the extrusion profile and extrusion time of each strut are analogous to the slew maneuver profile and slew time. Previous work [16] has emphasized how both the slew maneuver profile and the ratio between the slew time and fundamental natural period determine the magnitude of the resulting structural vibrations. Hence, our approach to safeguarding against the effects of flexible body dynamics during ISM is twofold: (1) we assume that each strut is smoothly extruded using the polynomial profile from Ref. [16] and (2) we constrain the extrusion time for each strut to be greater than or equal to ten times the fabricated structure's fundamental natural period, i.e., SF = 10.

The next two sections use these constraints to develop analytical and numerical frameworks to estimate the fabrication times of truss structures. These frameworks are then used to construct fabrication time diagrams in Secs. 3 and 4 to understand the dominant constraints on fabrication time for specific reticulated geometries as a function of their diameter D and strut length-to-diameter ratio L/D. These two parameters represent the overall dimension of the support structure and its average facet size, which controls how closely the reticulated geometry approximates the desired curved shape of the payload. For applications such as RF mesh reflectors and space telescopes which require paraboloid geometries, a large facet size (i.e., large L/D) results in greater root-mean-square (RMS) surface error [17]. For simplicity, we also only consider the fabrication time for extrusion of each strut; the time required,
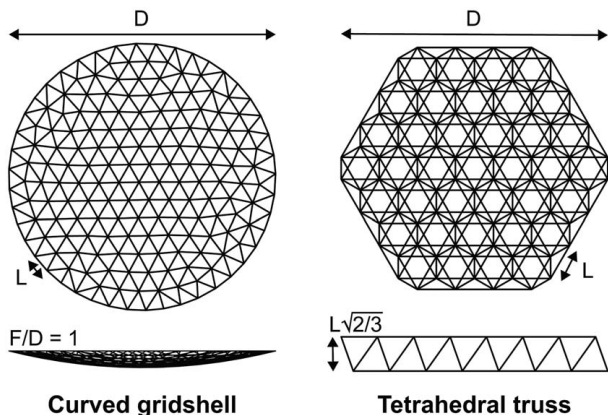
for example, for attaching joints or assembling the payload on the support structure are outside the scope of this paper.

2.1 Analytical Framework.
To predict fabrication times subject to the above constraints, we derive expressions for fabrication time considering each constraint separately: maximum fabrication power, maximum ACS torque and angular momentum storage, and flexible body dynamics. The critical fabrication time is then the maximum fabrication time amongst the four constraints.

2.1.1 Maximum Fabrication Power.
The maximum power available to the fabrication process, $P_{\max}$, limits the extrusion time of strut n as [12]

$$\Delta t_{\text{power}}(n) = \frac{u \rho A L}{P_{\max}} \tag{1}$$

where u is the specific energy consumption of the fabrication process, ρA is the linear mass density of the strut, and L is the average strut length. Equation (1) assumes that the spacecraft supplies constant, continuous power during the extrusion step. For multiple spacecraft simultaneously fabricating an equal fraction of the total number of struts, the total fabrication time is

$$T_{\text{power}} = \sum_{n=1}^{N/N_{SC}} \Delta t_{\text{power}}(n) = \frac{u}{P_{\max}} \frac{\rho A L N}{N_{SC}} \tag{2}$$

where N is the total number of struts in the geometry and N_{SC} is the number of spacecraft. For reticulated geometries such as the curved gridshell and tetrahedral truss, the total number of struts in the geometry approximately scales with the ratio of strut length-to-diameter [18] as

$$N \approx \frac{k}{(L/D)^2} \tag{3}$$

where k is a geometry-dependent coefficient (e.g., $k_{\text{gridshell}} = \pi\sqrt{3}/2$ and $k_{\text{tetra}} = 3\pi\sqrt{3}/2$). Substituting Eq. (3) into Eq. (2) yields the following expression for the total power-constrained fabrication time:

$$T_{\text{power}} = k\left(\frac{u}{P_{\max}N_{SC}}\right)\left(\frac{D}{L/D}\right)(\rho A) \tag{4}$$

2.1.2 Maximum Attitude Control System Torque and Angular Momentum Storage.
To estimate fabrication times constrained by the maximum ACS torque $\tau_{\max}$ and angular momentum storage $h_{\max}$, we compute the torque and angular momentum required to maintain the spacecraft in an inertially fixed orientation using variable-mass rigid body dynamics [19]. We model the spacecraft and fabricated structure during the fabrication process as a single, constant mass rigid body with time-varying geometry and mass distribution. This approach is consistent with our flexible body dynamics constraint in that we assume the fabrication is slow enough such that the structure behaves as a rigid body. The variable-mass rigid body dynamics therefore capture the essential physics by modeling the forces and torques from the changing geometry and mass distribution during each extrusion step.

The model is summarized as follows. For each spacecraft, as the number of struts in the fabricated structure increases from $n = 1$ to $n = N/N_{SC}$, the spacecraft mass $m_{SC}(n)$ decreases and the structure mass $m_T(n)$ increases such that their sum remains constant:

$$m_T(n) = \rho A L n \tag{5}$$

$$m_{SC}(n) = m_{SC0} + \rho A L\left(\frac{N}{N_{SC}} - n\right) \tag{6}$$

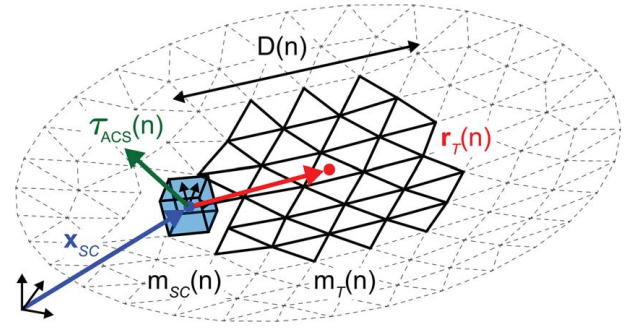$$M = m_T(n) + m_{SC}(n) = m_{SC0} + \frac{\rho A L N}{N_{SC}} \tag{7}$$

Fig. 2 Variable-mass rigid body dynamics model of a spacecraft during fabrication of a large truss structure. Momentum actuators apply a torque $\tau_{\text{ACS}}(n)$ to maintain a fixed orientation during extrusion of each strut.

Here, m_{SC0} is the mass of the spacecraft bus (i.e., the total mass of the spacecraft excluding the strut feedstock) and M is the mass of the combined rigid body.

During each extrusion step, the forces and torques from the changing geometry and mass distribution are calculated using the moment arm from the center of mass of the spacecraft to the center of mass of the fabricated structure ($\mathbf{r}_T$), the velocity ($\mathbf{v}_T$) and acceleration ($\mathbf{a}_T$) of the structure relative to the spacecraft, and the rates of change in mass distribution ($\dot{m}_T$, $\ddot{m}_T$). To maintain a fixed orientation with respect to inertial space, i.e., to maintain zero angular velocity and acceleration ($\boldsymbol{\omega} = \mathbf{0}$, $\dot{\boldsymbol{\omega}} = \mathbf{0}$), momentum actuators apply a torque during each extrusion step (τ_{ACS}), as shown in Fig. 2. With zero external forces and torques, the resulting force and moment equilibria are

$$\sum \mathbf{F} = M\ddot{\mathbf{x}}_{SC} + \ddot{m}_T \mathbf{r}_T + 2\dot{m}_T \mathbf{v}_T + m_T \mathbf{a}_T = \mathbf{0} \tag{8}$$

$$\sum \mathbf{M} = m_T \mathbf{r}_T \times \ddot{\mathbf{x}}_{SC} + \mathbf{r}_T \times (\dot{m}_T \mathbf{v}_T + m_T \mathbf{a}_T) + \tau_{\text{ACS}} = \mathbf{0} \tag{9}$$

Here, $\mathbf{x}_{SC}$ is the position of the spacecraft in inertial space and dot notation denotes differentiation with respect to time t. Appendix A derives Eqs. (8) and (9) from the equations of motion for a variable-mass system [19]. In the derivation, the mass moment of inertia terms multiply zero angular velocity and acceleration terms due to the assumption of an inertially fixed orientation, and hence, do not appear in Eqs. (8) and (9).

In Eq. (8), the forces from the time-varying geometry and mass distribution induce relative motion of the center of mass of the spacecraft ($\ddot{\mathbf{x}}_{SC} \neq \mathbf{0}$). However, the combined center of mass of the spacecraft and fabricated structure does not translate due to the lack of external forces. Substituting Eq. (8) into Eq. (9) and assuming the torques from mass redistribution are small compared to those from the relative motion of the fabricated structure, we obtain an expression for the required control torque $\tau_{\text{ACS}}(n)$ during the extrusion of strut n. Integrating this equation with respect to time then yields an approximation for the required angular momentum storage $\mathbf{h}_{\text{ACS}}(n)$ to maintain a fixed orientation:

$$\tau_{\text{ACS}}(n) \approx m_T(n)\mathbf{a}_T(n) \times \left(1 - \frac{m_T(n)}{M}\right)\mathbf{r}_T(n) \tag{10}$$

$$\mathbf{h}_{\text{ACS}}(n) \approx m_T(n)\mathbf{v}_T(n) \times \left(1 - \frac{m_T(n)}{M}\right)\mathbf{r}_T(n) \tag{11}$$

Equations (10) and (11) model the fabrication process as a series of discrete extrusion steps as n increases. To estimate the total constrained fabrication time, we assume each extrusion step follows a continuous profile with smooth derivatives. Specifically, we
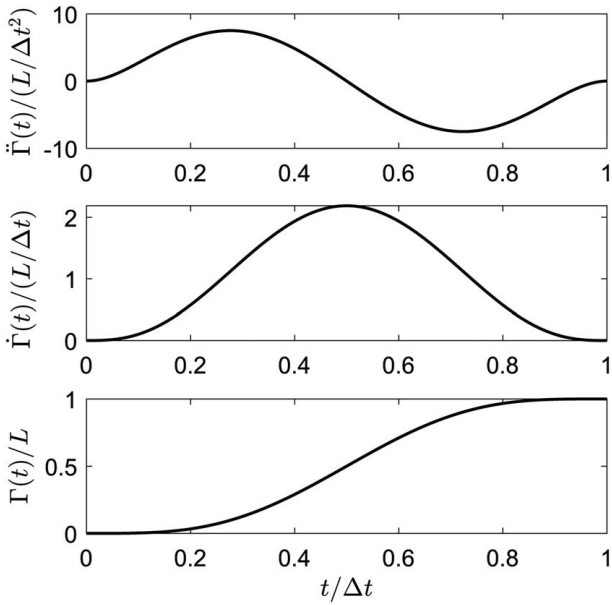
Fig. 3 Smooth extrusion profile $\Gamma(t)$ from Ref. [16] for a strut of length L over the period $t \in [0, \Delta t]$

assume that the instantaneous strut length follows a polynomial profile $\Gamma(t)$ over the period $t \in [0, \Delta t]$ with zero velocity, acceleration, and jerk at the end points (Fig. 3)[16]:

$$\Gamma(t) = \frac{-20L}{\Delta t^7}t^7 + \frac{70L}{\Delta t^6}t^6 + \frac{-84L}{\Delta t^5}t^5 + \frac{35L}{\Delta t^4}t^4 \qquad (12)$$

Using this extrusion profile, the maximum velocity and acceleration of the fabricated structure during each extrusion step are

$$\max\left(\|\mathbf{v}_T(n)\|_2\right) \approx \dot{\Gamma}_{\max} = \frac{35L}{16\Delta t} \qquad (13)$$

$$\max\left(\|\mathbf{a}_T(n)\|_2\right) \approx \ddot{\Gamma}_{\max} = \frac{84\sqrt{5}L}{25\Delta t^2} \qquad (14)$$

Additionally, for reticulated geometries such as the curved grid-shell, we assume that the maximum moment arm from the spacecraft scales with the radius of the fabricated structure and the square root of the number of struts in accordance with Eq. (3):

$$\max\left(\|\mathbf{r}_T(n)\|_2\right) \approx \frac{D(n)}{2} = \frac{L}{2}\sqrt{\frac{n}{k}} \qquad (15)$$

Substituting Eqs. (13)–(15) into Eqs. (10) and (11) yields expressions that relate the magnitudes of the maximum control torque and angular momentum storage ($\tau_{\max}$, $h_{\max}$) of the spacecraft with the associated constrained extrusion times (Δt_{torque}, Δt_{mom}) of strut n:

$$\tau_{\max} \approx \left(m_T(n)\frac{84\sqrt{5}L}{25\Delta t_{\text{torque}}(n)^2}\right)\left(1 - \frac{m_T(n)}{M}\right)\left(\frac{L}{2}\sqrt{\frac{n}{k}}\right) \qquad (16)$$

$$h_{\max} \approx \left(m_T(n)\frac{35L}{16\Delta t_{\text{mom}}(n)}\right)\left(1 - \frac{m_T(n)}{M}\right)\left(\frac{L}{2}\sqrt{\frac{n}{k}}\right) \qquad (17)$$

Equations (16) and (17) assume that the moment arm from the spacecraft to the fabricated structure is always perpendicular to the direction of strut extrusion and that the maximum velocity and acceleration of each extrusion coincide at the same instant in time. These assumptions likely overestimate the required control torque and angular momentum storage because the moment arm

may not be perpendicular to the extrusion direction at each step and the maximum velocity and acceleration occur at different instants in time during the extrusion profile (cf. Fig. 3). Substituting Eq. (5) into Eqs. (16) and (17) and rearranging for the constrained fabrication times yield

$$\Delta t_{\text{torque}}(n) \approx \sqrt{\frac{42\sqrt{5}\rho AL^3 n^{3/2}(1 - \rho ALn/M)}{25k^{1/2}\tau_{\max}}} \qquad (18)$$

$$\Delta t_{\text{mom}}(n) \approx \frac{35\rho AL^3 n^{3/2}(1 - \rho ALn/M)}{32k^{1/2}h_{\max}} \qquad (19)$$

To obtain the total constrained fabrication time for multiple spacecraft simultaneously fabricating an equal fraction of the total number of struts, we sum over n and approximate the sums as definite integrals, i.e.,

$$T_{\text{torque}} = \sum_{n=1}^{N/N_{SC}} \Delta t_{\text{torque}}(n) \approx \int_0^{N/N_{SC}} \Delta t_{\text{torque}}(n)\,dn \qquad (20)$$

$$T_{\text{mom}} = \sum_{n=1}^{N/N_{SC}} \Delta t_{\text{mom}}(n) \approx \int_0^{N/N_{SC}} \Delta t_{\text{mom}}(n)\,dn \qquad (21)$$

Equations (20) and (21) assume that the full ACS authority of the spacecraft is available for each extrusion step and neglect time for momentum desaturation. To further simplify Eqs. (20) and (21), we substitute Eqs. (3), (18), and (19) and compute a Laurent-Puiseux series expansion in L/D about $L/D = 0$ [20]. A Laurent-Puiseux series expansion is required here since the total fabrication times become unbounded near $L/D = 0$. We assume $L/D \ll 1$ and retain terms with $(L/D)^n$ where $n < 0$, resulting in the following expressions for the total fabrication times constrained by the maximum control torque $\tau_{\max}$ and momentum $h_{\max}$:

$$
\begin{aligned}
T_{\text{torque}} \approx & \left(\frac{1}{\tau_{\max}}\right)^{1/2}\left(0.619k^{3/2}\left(\frac{1}{N_{SC}}\right)^{7/4}\left(\frac{D^{3/2}}{(L/D)^2}\right)(\rho A)^{1/2}\right. \\
& + 1.08k^{1/2}\left(\frac{m_{SC0}}{N_{SC}^{3/4}}\right)\left(\frac{D^{1/2}}{L/D}\right)(\rho A)^{-1/2} \\
& \left. - 1.29\left(\frac{m_{SC0}}{N_{SC}^{1/4}}\right)\left(\frac{1}{L/D}\right)^{1/2}(\rho A)^{-1}\right)
\end{aligned}
\qquad (22)
$$

$$
\begin{aligned}
T_{\text{mom}} \approx & \left(\frac{1}{h_{\max}}\right)\left(\frac{k^2}{8}\left(\frac{1}{N_{SC}}\right)^{5/2}\left(\frac{D^3}{(L/D)^2}\right)(\rho A)\right. \\
& \left. + \frac{5k}{16}\left(\frac{m_{SC0}}{N_{SC}^{3/2}}\right)\left(\frac{D^2}{L/D}\right)\right)
\end{aligned}
\qquad (23)
$$

2.1.3 Flexible Body Dynamics. The flexible body dynamics during fabrication will constrain the extrusion time of strut n as

$$\Delta t_{\text{flex}}(n) = \frac{\text{SF}}{f_0(n)} \qquad (24)$$

where $f_0(n)$ is the fundamental natural frequency of the fabricated structure and SF is a multiplicative safety factor. To estimate $f_0(n)$, we model the fabricated structure using a single vibration mode for a clamped-free cantilever beam with a tip mass and tip inertia; the clamped end of the beam represents its connection to the spacecraft (Fig. 4). This approach assumes that the kinetic energy during vibration is exchanged with the strain energy from the deformation of a few struts near the clamped node, which is subsequently validated with finite element modeling in the numerical framework (Sec. 2.2).
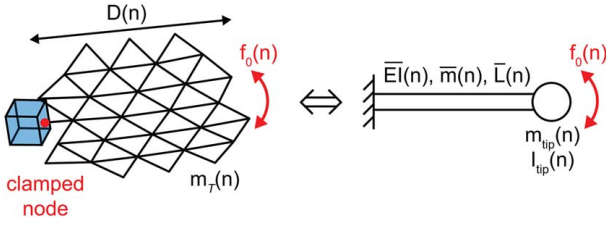
Fig. 4 Fundamental vibration mode of the fabricated structure with *n* struts and equivalent clamped-free cantilever beam vibration mode with tip mass and tip inertia

To derive the effective properties of the cantilever beam, we model a beam of length $\overline{L}(n)$ and linear mass density $\overline{m}(n)$ which scale with the radius and mass of the fabricated structure. Given the assumption of a clamped-free vibration mode, we model the beam bending stiffness, $\overline{EI}(n)$, as the bending stiffness of each strut, EI, multiplied by the mean connectivity of the fabricated structure, $\kappa(n)$. The connectivity $\kappa(n)$ represents the average number of struts at each node, and we assume it linearly increases during the fabrication process from $\kappa = 1$ to $\kappa = \kappa_0$ where κ_0 is the mean connectivity of the final reticulated geometry (e.g., $\kappa_{0\text{gridshell}} = 6$, $\kappa_{0\text{tetra}} = 9$). We model the tip mass $m_{\text{tip}}(n)$ as the total mass of the fabricated structure and the tip inertia $I_{\text{tip}}(n)$ as the polar moment of inertia of a circular disk with equivalent diameter and mass. The natural frequency of the clamped-free cantilever beam is then given by [21]

$$f_0(n) = \frac{\beta_0}{2\pi \overline{L}(n)^2}\sqrt{\frac{\overline{EI}(n)}{\overline{m}(n)}} \tag{25}$$

where β_0 is the solution to the characteristic equation for a clamped-free beam with a tip mass and tip inertia at the free end [21]:

$$\overline{L}^4\overline{m}^2 + I_{\text{tip}}m_{\text{tip}}\beta_0^2 + \left(\overline{L}^4\overline{m}^2 - I_{\text{tip}}m_{\text{tip}}\beta_0^2\right)\cos\left(\sqrt{\beta_0}\right)\cosh\left(\sqrt{\beta_0}\right)$$
$$- \overline{L}\,\overline{m}\sqrt{\beta_0}\left(\overline{L}^2 m_{\text{tip}} + I_{\text{tip}}\beta_0\right)\sin\left(\sqrt{\beta_0}\right)\cosh\left(\sqrt{\beta_0}\right)$$
$$+ \overline{L}\,\overline{m}\sqrt{\beta_0}\left(\overline{L}^2 m_{\text{tip}} - I_{\text{tip}}\beta_0\right)\cos\left(\sqrt{\beta_0}\right)\sinh\left(\sqrt{\beta_0}\right) = 0 \tag{26}$$

Substituting the effective properties of the cantilever beam summarized in Appendix B into Eq. (26), we find that the fundamental natural frequency corresponds to $\beta_0 \approx 1.087$. Then, substituting Eq. (25) into Eq. (24), we find the constrained extrusion time of strut n as

$$\Delta t_{\text{flex}}(n) \approx \text{SF}\sqrt{\frac{4.17\rho A L^4 n^{5/2}}{k^{3/2}\kappa(n)EI}} \tag{27}$$

Therefore, the total constrained fabrication time for multiple spacecraft simultaneously fabricating an equal fraction of the total number of struts is

$$T_{\text{flex}} = \sum_{n=1}^{N/N_{SC}} \Delta t_{\text{flex}}(n) \approx \int_0^{N/N_{SC}} \Delta t_{\text{flex}}(n)\,dn \tag{28}$$

To simplify Eq. (28), we substitute Eqs. (3) and (27) and take a Laurent-Puiseux series expansion in L/D about the indeterminate point $L/D = 0$, for the same reasons as before [20]. Again we assume $L/D \ll 1$ and retain terms with $(L/D)^n$ where $n < 0$, resulting in the following expression for the total constrained fabrication time:

$$T_{\text{flex}} \approx 0.908\text{SF}\left(\frac{C_1 D^2}{N_{SC}^{9/4}(L/D)^{5/2}} + \frac{C_2 D^2}{N_{SC}^{5/4}(L/D)^{1/2}}\right)\left(\frac{\rho A}{EI}\right)^{1/2} \tag{29}$$

Table 1 Total constrained fabrication times from analytical framework

Maximum fabrication power—Eq. (4):

$$T_{\text{power}} = k\left(\frac{u}{N_{SC}P_{\text{max}}}\right)\left(\frac{D}{L/D}\right)(\rho A)$$

Maximum ACS torque—Eq. (22):

$$T_{\text{torque}} \approx \left(\frac{1}{\tau_{\text{max}}}\right)^{1/2}\left(0.619k^{5/4}\left(\frac{1}{N_{SC}}\right)^{7/4}\left(\frac{D^{3/2}}{(L/D)^2}\right)(\rho A)^{1/2} + \right.$$
$$\left. 1.08k^{1/2}\left(\frac{m_{SC0}}{N_{SC}^{3/4}}\right)\left(\frac{D^{1/2}}{L/D}\right)(\rho A)^{-1/2} - 1.29\left(\frac{m_{SC0}}{N_{SC}^{1/4}}\right)\left(\frac{1}{L/D}\right)(\rho A)^{-1}\right)$$

Maximum ACS angular momentum storage—Eq. (23):

$$T_{\text{mom}} \approx \left(\frac{1}{h_{\text{max}}}\right)\left(\frac{k^2}{8}\left(\frac{1}{N_{SC}}\right)^{5/2}\left(\frac{D^3}{(L/D)^2}\right)(\rho A) + \frac{5k}{16}\left(\frac{m_{SC0}}{N_{SC}^{3/2}}\right)\left(\frac{D^2}{L/D}\right)\right)$$

Flexible body dynamics—Eq. (29):

$$T_{\text{flex}} \approx 0.908\text{SF}\left(\frac{C_1 D^2}{N_{SC}^{9/4}(L/D)^{5/2}} + \frac{C_2 D^2}{N_{SC}^{5/4}(L/D)^{1/2}}\right)\left(\frac{\rho A}{EI}\right)^{1/2}$$

where the constants C_1, C_2 are given in terms of the coefficients k, κ_0, and the hypergeometric function ${}_2F_1$ as

$$C_1 = k^{3/2}\kappa_0^{1/2}\,{}_2F_1\left(1, \frac{11}{4}, \frac{13}{4}, 1 - \kappa_0\right) \tag{30}$$

$$C_2 = \frac{1 - \kappa_0}{k}C_1 - \frac{11k^{1/2}\kappa_0^{3/2}}{13}\,{}_2F_1\left(2, \frac{15}{4}, \frac{17}{4}, 1 - \kappa_0\right) \tag{31}$$

2.1.4 Summary of Analytical Framework. Table 1 summarizes the equations for the constrained fabrication times of a truss structure with diameter D and strut length-to-diameter ratio L/D. The parameters that enter the equations of Table 1 are classified as: the number of spacecraft (N_{SC}), the spacecraft properties (m_{SC0}, P_{max}, τ_{max}, h_{max}), the fabrication process properties (u), the strut properties (ρA, EI), and the truss geometry (D, L/D, k, κ_0). The effects of these model parameters on total fabrication time are discussed in Sec. 4.

2.2 Numerical Framework. To validate the analytical framework, we develop a numerical framework for computing fabrication times for ISM of truss structures subject to the same four constraints. Instead of using the geometrical approximations inherent to the equations in Table 1, we use the actual truss geometry, a specific fabrication sequence, and finite element modeling to arrive at higher-fidelity fabrication time estimates.

We first generate the geometries of the truss structures (Fig. 1). For the curved gridshell, we use the open-source software DISTMESH [22] to create a flat, triangular mesh with average strut length L inside a circle of diameter D, and vertically offset the nodes to form a paraboloid with focal length-to-diameter ratio $F/D = 1$. For the tetrahedral truss, we tessellate the octahedral unit cell with sidelength L to create a hexagonal structure with corner-to-corner diameter D. Next, we select a path that traverses all the edges of the truss geometry and represents the specific fabrication sequence of struts. The resulting paths are known as Euler paths [23], and they are compatible with extrusion-based fabrication processes which fabricate the structure as a single unit (e.g., bend-forming [11]). Euler paths can also represent a continuous assembly sequence of pre-fabricated struts. Here, we compute a radially expanding Euler path from a randomly selected starting node using the algorithm summarized in Appendix C, which is based on the Fluery algorithm [23]. This fabrication path dictates the geometry of the truss structure after each extrusion step and is used to compute the total constrained fabrication time.

2.2.1 Maximum Fabrication Power. The only differences between the analytical and numerical framework for the maximum power constraint is the total number of struts and the individual strut lengths. Whereas the analytical framework uses the average strut length and an approximation for the total number of struts (Eq. (3)), the numerical framework uses the actual strut lengths $L(n)$ and the total number of struts N in the meshed geometry (equally partitioned amongst the N_{SC} spacecraft):

$$T_{\text{power}} = \frac{u}{P_{\max}} \frac{\rho A N}{N_{SC}} \sum_{n=1}^{N/N_{SC}} L(n) \qquad (32)$$

2.2.2 Maximum Attitude Control System Torque and Angular Momentum Storage. The numerical framework uses variable-mass rigid body dynamics to compute the required control torque and angular momentum storage to maintain a fixed orientation during each extrusion step. However, we directly use the geometry and mass distribution of the spacecraft and fabricated structure following the specified fabrication path, removing the additional simplifying assumptions of Sec. 2.1.2. To this end, we compute the mass, center of mass, and geometry of the fabricated structure before and after each extrusion step, and compute the required control torque $\tau_{\text{ACS}}(n, \Delta t)$ during extrusion of strut n using Eqs. (8) and (9). We assume that the moment arm, velocity, acceleration, and mass of the structure all follow the polynomial profile of Eq. (12) over the extrusion period Δt and numerically integrate the control torque to obtain the angular momentum storage $\boldsymbol{h}_{\text{ACS}}(n, \Delta t)$. To find the constrained fabrication times, we solve for Δt which minimizes the difference between the required control torque and angular momentum storage and the ACS capabilities of the spacecraft:

$$\Delta t_{\text{torque}}(n) = \operatorname*{argmin}_{\Delta t} \left\| \tau_{\max} \mathbf{1} - \boldsymbol{\tau}_{\text{ACS}}(n, \Delta t) \right\|_\infty \qquad (33)$$

$$\Delta t_{\text{mom}}(n) = \operatorname*{argmin}_{\Delta t} \left\| h_{\max} \mathbf{1} - \mathbf{h}_{\text{ACS}}(n, \Delta t) \right\|_\infty \qquad (34)$$

Equations (33) and (34) assume equally capable momentum actuators about all three axes. At each extrusion step, we numerically solve these equations for the constrained fabrication time using the damped least-squares method [24] and then sum over all the steps to obtain the total fabrication time.

2.2.3 Flexible Body Dynamics. The numerical framework uses the natural frequency-based constraint on fabrication time from the analytical framework (Eq. (24)) to minimize the effects of flexible body dynamics during strut extrusion. However, whereas the analytical framework estimates natural frequencies from an equivalent cantilever beam model, the numerical framework computes the fundamental clamped-free natural frequencies using flexible multibody dynamics finite element models at each step along the specified fabrication path.

In the numerical framework, we model the fabricated structure using the flexible multibody dynamics finite element modeling paradigm and associated MATLAB implementation from Ref. [25]. Each member in the fabricated structure is modeled as a thin-walled cylindrical tube with appropriate material and geometric properties (see Table 2). The members are then discretized using the quaternion-based geometrically nonlinear Timoshenko beam finite elements from Ref. [25]. These elements are a structure-preserving reformulation of the geometrically nonlinear Timoshenko beam finite elements originally introduced in Ref. [26] and are advantageous here because they allow complex geometries and joint constraints to be modeled in a single global reference frame [25]. The shear stiffnesses for the Timoshenko beam elements are approximated using the Timoshenko shear correction factor for a thin-walled cylindrical tube [27]. Our formulation exactly integrates the translational inertia forces and approximates the rotational inertia forces using five-point Gaussian quadrature. It then approximates the internal elastic forces using one-point reduced integration

Table 2 Model parameters for fabrication time diagrams

Number of spacecraft:	
$\quad N_{SC} = 1$	
Spacecraft properties:	
$\quad m_{SC0} = 250\,\text{kg}$	
$\quad P_{\max} = 5\,\text{kW}$	
$\quad \tau_{\max} = 0.2\,\text{N\,m}$	
$\quad h_{\max} = 100\,\text{N\,ms}$	
Fabrication process:	
$\quad u = 0.5\,\text{MJ/kg}$	
Strut properties:	
$\quad \rho = 7800\,\text{kg/m}^3$	
$\quad E = 200\,\text{GPa}$	
$\quad d_o = 5\,\text{cm},\ t_o = 1\,\text{mm}$	
Truss-dependent coefficients:	
$\quad (k, \kappa_0)_{\text{gridshell}} = (\pi\sqrt{3}/2, 6)$	
$\quad (k, \kappa_0)_{\text{tetra}} = (3\pi\sqrt{3}/2, 9)$	

with MacNeal's residual bending flexibility correction [28] to alleviate shear locking [25,29]. Truss members are rigidly constrained to each other using the method of Lagrange multipliers [30].

For modal analyses, the flexible multibody dynamics models are clamped at their points of attachment to the spacecraft and linearized at rest in their undeformed configurations. The resulting linearized finite elements are equivalent to standard C_0 beam finite elements (see e.g., Ref. [29]). Galerkin projections onto the null spaces of the corresponding constraint gradient matrices then eliminate the constraints and convert the linearized finite element equations of motion into a standard form for modal analysis. The subsequent eigenproblems are solved using the subspace iteration method [31] with the generalized Jacobi method [31] to solve each subspace iteration's lower-dimensional eigenproblem. The subspace iteration method is initialized using the eigenvectors from a modal analysis with a randomly perturbed mass matrix to break any symmetries inherent to the eigenproblem. Empirical evidence shows that this symmetry breaking leads to improved accuracy and convergence for symmetric structures [25].

Mesh convergence studies for the gridshell and tetrahedral truss structures considered in this paper indicated that the fundamental natural frequencies typically converge with a minimum of three elements per strut, irrespective of both the strut length and the selected fabrication path. As a result, each strut is discretized with three elements in the subsequent numerical analyses.

2.3 Construction of Fabrication Time Diagrams. The four constraints modeled in Secs. 2.1 and 2.2 provide different estimates of the total fabrication time of truss structures as a function of the various model parameters. To find the critical fabrication time $\overline{T}$ for a given geometry, we compute the maximum fabrication time amongst the four constraints:

$$\overline{T} = \max\left(T_{\text{power}}, T_{\text{torque}}, T_{\text{mom}}, T_{\text{flex}} \right) \qquad (35)$$

The constraint that yields the critical fabrication time then represents the dominant constraint for that geometry. In this way, the above analysis can create fabrication time diagrams which plot the dominant constraints and the critical fabrication times for a wide range of dimensions. These diagrams are useful for visualizing the effects of dominant constraints and understanding the effects of model parameters, as further described in Secs. 3 and 4.

3 Representative Fabrication Time Diagrams

We construct fabrication time diagrams for the ISM of two representative reticulated geometries: the curved gridshell and
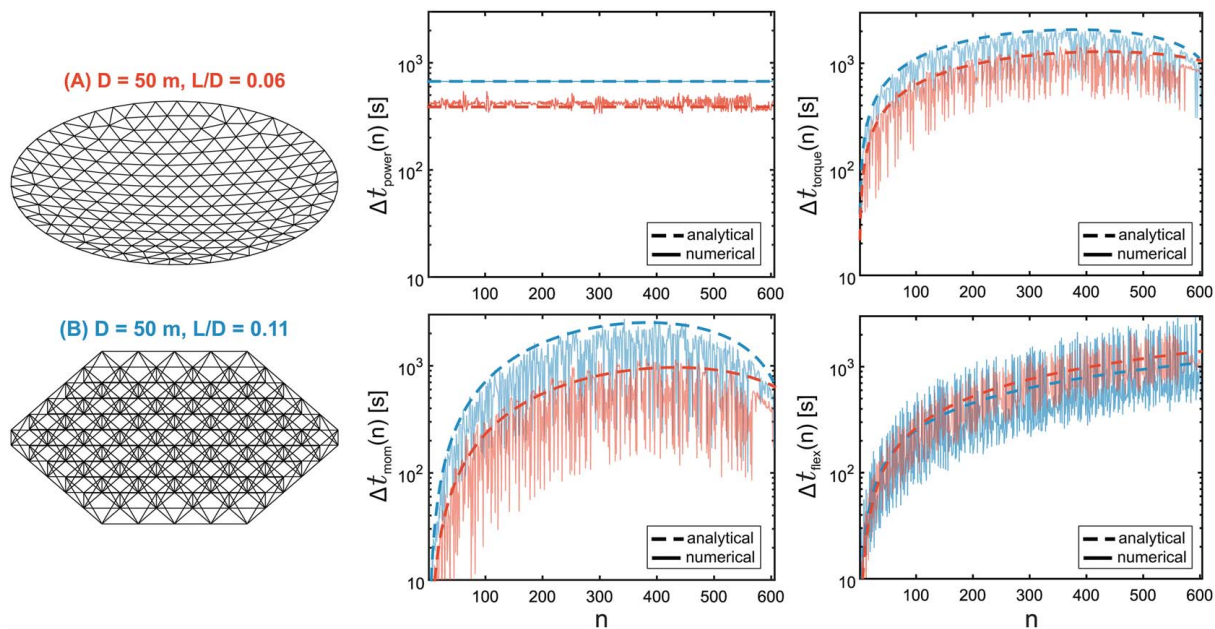
Fig. 5 Constrained extrusion times of each strut during the fabrication of a curved gridshell (A) and tetrahedral truss (B)

tetrahedral truss (Fig. 1). Specifically, we select the model parameters of Table 2 to represent the ISM of a truss structure from steel tubes via deformation processing. Using the analysis in Sec. 2, we compute the constrained fabrication times for the range of

diameters $D \in [10, 200]$ m and strut length-to-diameter ratios $L/D \in [0.25, 0.05]$, summarized in Figs. 5 and 6.

The constrained fabrication times in Figs. 5 and 6 show good agreement between the analytical and numerical frameworks. In
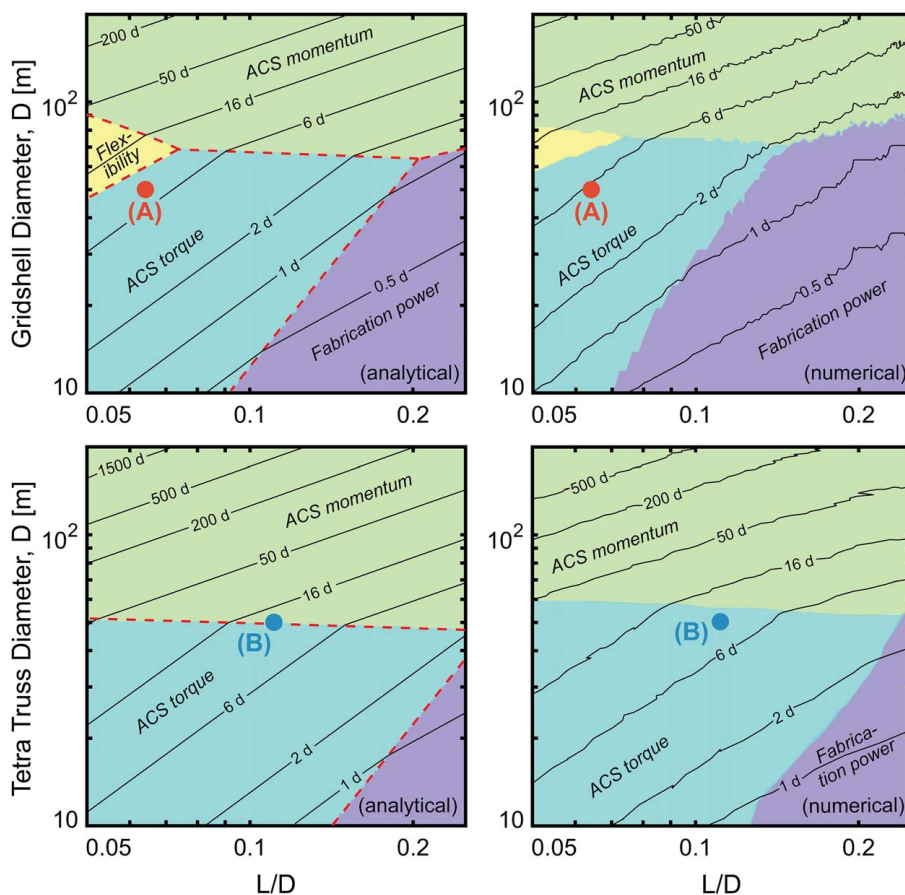

Fig. 6 Fabrication time diagrams for ISM of curved gridshells and tetrahedral trusses with varying diameter D and strut length-to-diameter ratio L/D. The regions indicate dominant constraints with overlaid contours of fabrication time in days. The labeled points correspond to the results in Fig. 5.

Fig. 5, we see the effects of each constraint as the number of struts in the fabricated structure increases. For the maximum power constraint, the fabrication time of each strut is solely controlled by the ratio of the specific energy consumption to the maximum power ($u/P_{\max}$) and does not vary with the size of the fabricated structure. The small differences between the analytical and numerical frameworks are due to the differences between the actual strut lengths in the numerical framework and the average strut length assumed in the analytical one.

For the ACS constraints, the fabrication time initially increases with the number of struts but plateaus and decreases at the end of fabrication for these specific geometries. The initial increase in fabrication time with the number of struts results from the larger mass and moment arm of the fabricated structure from the spacecraft, requiring greater ACS torque and angular momentum storage to maintain orientation. However at the end of fabrication, the truss mass is a large fraction of the total mass, resulting in a larger acceleration of the spacecraft ($\ddot{\mathbf{x}}_{SC}$) in the opposite direction as the truss during each extrusion step. For sufficiently large fractions of truss mass to total mass ($m_T/M \approx 1$), the required ACS torque and angular momentum storage decrease following the quadratic relationship between the ACS authority and truss mass in Eqs. (10) and (11). This causes a corresponding decrease in ACS-constrained extrusion times at the end of fabrication, as evident from Fig. 5. Additionally, Fig. 5 shows that the analytical framework generally overestimates the fabrication times for these constraints, demonstrating that the assumptions of Sec. 2.1.2 regarding the maximum moment arm and relative motion of the fabricated structure are indeed conservative.

For the flexibility constraint, the fabrication time tends to increase during fabrication due to the decreasing fundamental natural frequency of the fabricated structure. The analytical model of the clamped-free cantilever beam captures the trend of decreasing fundamental natural frequency; however, the numerical results from the finite element model show a larger spread in Figs. 5 and 6. The larger spread is the result of the different assumptions in the analytical and numerical models; the former computes the natural frequencies for a fabricated structure that grows radially and uniformly (Eq. (15)), whereas the latter computes them for a structure following a specific radially expanding fabrication path. Interestingly, although the tetrahedral truss has a larger equivalent bending stiffness than the gridshell [17], the flexibility-constrained fabrication times grow at similar rates due to the common fundamental vibration mode that is governed by the deformation of struts near the clamped node. The good agreement between the analytical and numerical frameworks for the flexibility constraint validates the assumptions of the clamped-free cantilever beam model of Sec. 2.1.3.

The fabrication time diagrams of Fig. 6 provide insights into the dominant constraints on fabrication time for the given range of dimensions. For relatively small and coarse gridshell geometries ($D < 60$ m, $L/D > 0.1$), the fabrication power dominates, i.e., the fabrication is slow enough that the spacecraft maintains a fixed orientation with the available ACS authority and the flexible body dynamics are negligible. The ACS torque becomes dominant for denser geometries ($D < 60$ m, $L/D < 0.1$) as the increased truss mass requires a greater torque to maintain a fixed orientation during each extrusion step. For larger diameters ($D > 60$ m), the angular momentum storage drives the fabrication time due to the increased mass and larger moment arms of the fabricated structures. The flexible body dynamics constraint only dominates within a small range of dimensions ($D \in [60, 80]$ m, $L/D < 0.07$) where the lower natural frequencies of the structure require greater fabrication times to avoid control–structure interactions. For the tetrahedral truss, we see a similar transition at $D \approx 45$ m from the fabrication power and ACS torque constraints to the angular momentum constraint. This transition occurs at a smaller diameter than for the gridshell because the tetrahedral truss is more massive than the gridshell for the same diameter D and strut length-to-diameter ratio L/D.

For the spacecraft and feedstock parameters of Table 2, the fabrication time contours in Fig. 6 suggest that 100-m diameter gridshells can be fabricated within a month via deformation processing of steel tubes, whereas tetrahedral trusses with similar diameters require fabrication over multiple months. The contours highlight the different scaling between the truss geometry and the fabrication time for each constraint. For the fabrication power constraint, the fabrication time scales with a slope of unity, i.e., proportional to the truss mass. For the angular momentum constraint, the fabrication time scales with a shallower slope of approximately 2/3, whereas for the flexibility and ACS torque constraints, the fabrication time scales with steeper slopes of 5/4 and 4/3, respectively. The largest slope for the ACS torque constraint shows that decreasing the L/D ratio for that range of dimensions results in the greatest increase in fabrication time.

The fabrication time contours in Fig. 6 also show the size limits of structures that can be feasibly constructed within a given fabrication time. For instance, three gridshells—$(D, L/D) = (40$ m, $0.06)$, $(70$ m, $0.1)$, $(100$ m, $0.18)$—can all be constructed in six days via deformation processing of steel tubes. In other words, smaller truss structures with smaller L/D ratios can be built in the same time as larger truss structures with larger L/D ratios. This design tradeoff between the overall dimension and average facet size of the support structure indicates that one approach for decreasing fabrication times is to fabricate a coarser geometry with a larger L/D ratio and use active control or shape correction to decrease the RMS surface error. For applications such as RF mesh reflectors, electrostatic actuation is a promising candidate for such active control due to its low mass, low power, and compatibility with distributed actuators attached to the support structure [32].

4 Utility of Fabrication Time Diagrams

We illustrate the utility of fabrication time diagrams by studying the effects of various model parameters, such as the fabrication speed and ACS authority of the spacecraft, on the total fabrication times of truss structures. Using the equations of Table 1 and the parameters of Table 2, the sections below highlight the effects of each model parameter on the total fabrication time of curved gridshells over a range of dimensions.

4.1 Effect of Spacecraft Bus Mass. Figure 7 shows the effects of the spacecraft bus mass, i.e., the mass of the spacecraft excluding the strut feedstock, on the fabrication times of curved gridshells. Increasing the spacecraft bus mass between $m_{SC0} \in [10^2, 10^4]$ kg increases the control torque and angular momentum storage required to maintain a fixed orientation during each extrusion step (Eqs. (16) and (17)), thereby increasing the dominance of the ACS constraints. The total fabrication times generally increase with the spacecraft bus mass; however, Fig. 7 shows that increasing the spacecraft bus mass over two orders of magnitudes only increases the fabrication times in the ACS torque and angular momentum-constrained regions by a factor of less than two. This relatively small effect results from the simplifying assumptions of the variable-mass rigid body dynamics model (Sec. 2.1.2) in which the forces and torques during each extrusion step are dominated by the mass and relative motion of the fabricated structure, not the spacecraft. In the absence of external disturbances, the results in Fig. 7 show that minimizing bus mass minimizes the fabrication time. However, as the spacecraft mass and inertia increase, other considerations such as environmental disturbance torques may change these conclusions.

4.2 Effect of Attitude Control System Authority. Figure 8 shows the effects of varying the ACS torque and angular momentum storage of the spacecraft. The three panels represent momentum actuators with increasing capability: small reaction
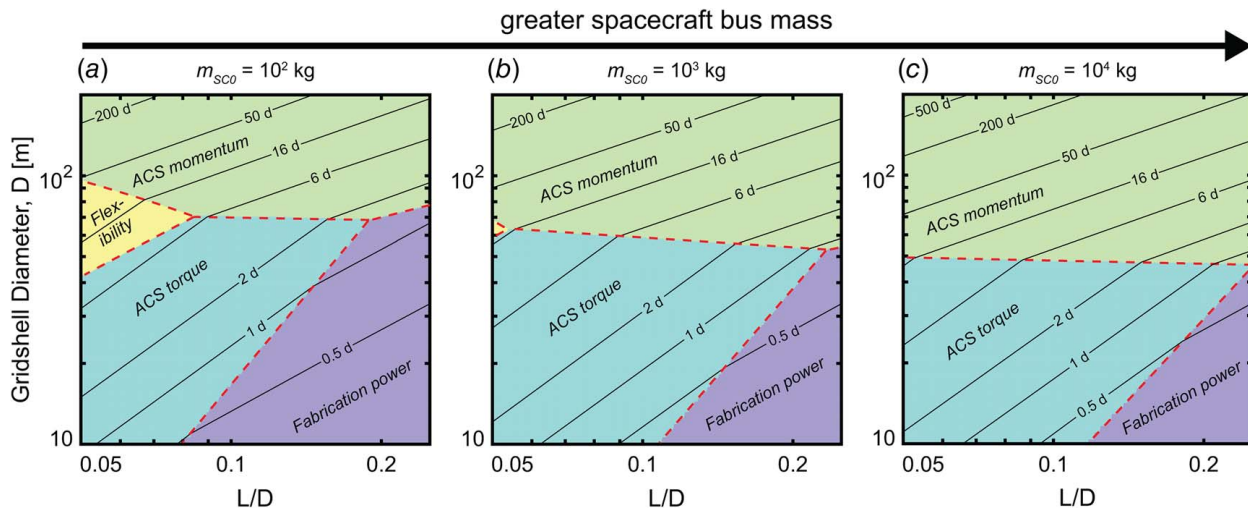
greater spacecraft bus mass

Fig. 7 Effect of spacecraft bus mass on the fabrication time of curved gridshells with varying diameter D and strut length-to-diameter ratio L/D
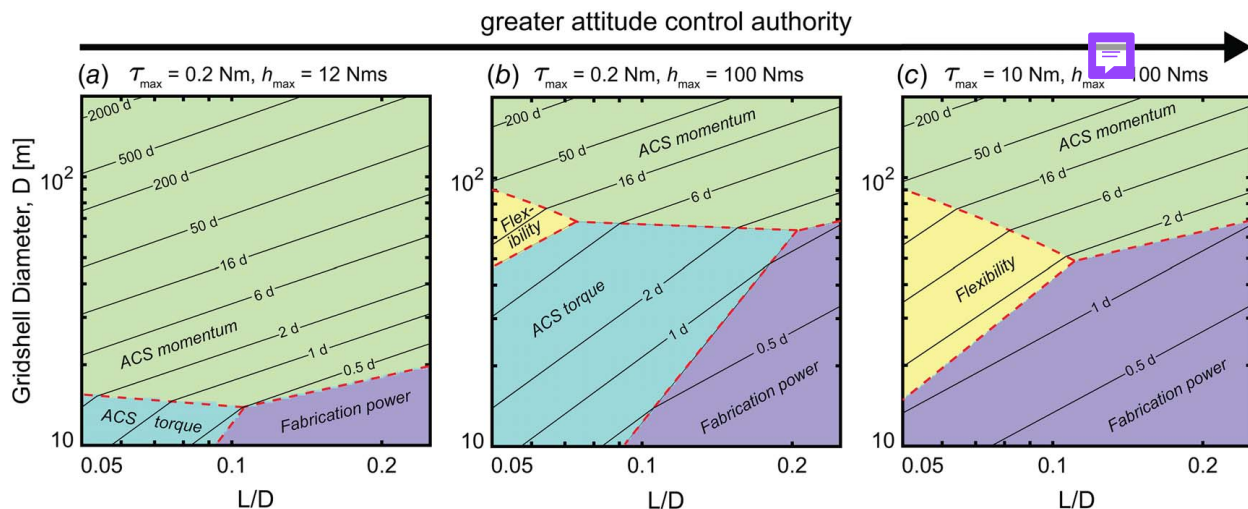
greater attitude control authority

Fig. 8 Effect of attitude control authority of the spacecraft on the fabrication time of curved gridshells with varying diameter D and strut length-to-diameter ratio L/D

wheels ($\tau_{max} = 0.2\,\text{N m}$, $h_{max} = 12\,\text{N ms}$),[2] large reaction wheels ($\tau_{max} = 0.2\,\text{N m}$, $h_{max} = 100\,\text{N ms}$) [16], and large control moment gyroscopes ($\tau_{max} = 10\,\text{N m}$, $h_{max} = 100\,\text{N ms}$) [33]. With small reaction wheels (Fig. 8(a)), the ACS torque and power constraints dominate below $D < 15\,\text{m}$, whereas the angular momentum constraint dominates for larger diameters and yields fabrication times of up to multiple years for 100-m diameter gridshells. With greater ACS authority, the ACS constraints become less strict and the fabrication times scale inversely with the available angular momentum storage and the square root of the available ACS torque (Eqs. (22) and (23)). With large control moment gyroscopes (Fig. 8(c)), the angular momentum storage still constrains the fabrication time of 100-m diameter gridshells to multiple months. Hence, the results in Fig. 8 suggest that to minimize fabrication time while maintaining a fixed orientation, the spacecraft should maximize ACS authority, particularly the available angular momentum storage.

4.3 Effect of Fabrication Speed. Figure 9 shows the effects of varying the fabrication speed, i.e., the ratio of fabrication power to the specific energy consumption, $P_{max}/u \in [10^{-3}, 10^{-1}]\,\text{kg/s}$. For a spacecraft with a power budget of $P_{max} = 5\,\text{kW}$, the panels of Fig. 9 represent three different fabrication processes: a melt-based extrusion process ($u \approx 5\,\text{MJ/kg}$), a deformation process ($u \approx 0.5\,\text{MJ/kg}$), and an ultra-efficient extrusion process ($u \approx 0.05\,\text{MJ/kg}$). The power constraint is most dominant for the melt-based process (Fig. 9(a)) and becomes less dominant as the fabrication speed increases (Figs. 9(b) and 9(c)). Additionally, the power constraint is generally only dominant for smaller, coarser geometries, as the ACS and flexibility constraints still dominate for larger, denser geometries. Comparing Fig. 9(b) to our analysis in Ref. [12] which considered solely the power constraint and estimated fabrication times of multiple days for 100-m diameter trusses via deformation processing, the fabrication times considering the additional ACS and flexible body dynamics constraints are an order of magnitude larger. Hence, the results in Fig. 9 suggest that increasing the available fabrication power only increases the rate of fabrication up until the point where other constraints (e.g., ACS authority and flexible body dynamics) begin to limit the fabrication time.
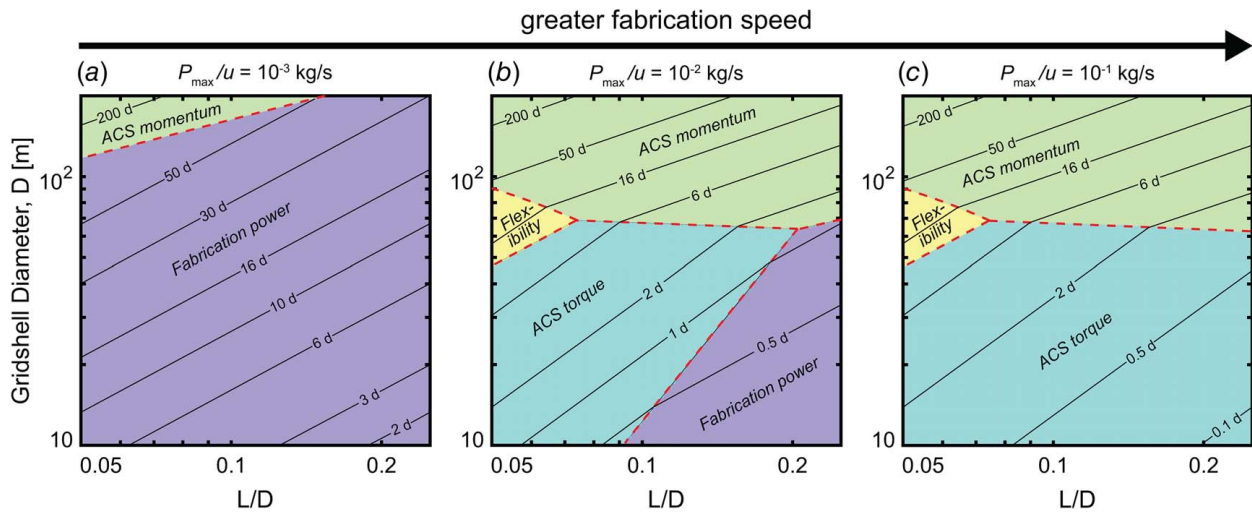
---

[2]https://www.rocketlabusa.com/space-systems/satellite-components/reaction-wheels/

Fig. 9 Effect of fabrication speed on the fabrication time of curved gridshells with varying diameter _D_ and strut length-to-diameter ratio _L/D_

4.4 Effect of Feedstock Material. Figure 10 shows the effects of varying the specific stiffness $\sqrt{E/\rho}$ of the feedstock material. The panels represent different feedstock materials and their respective fabrication processes: (a) deformation processing of copper tubes ($\sqrt{E/\rho} = 4 \cdot 10^3$ m/s, $P_{max}/u = 10^2$ kg/s); (b) deformation processing of steel tubes ($\sqrt{E/\rho} = 5 \cdot 10^3$ m/s, $P_{max}/u = 10^2$ kg/s); and (c) melt-based processing of CFRP tubes ($\sqrt{E/\rho} = 1.4 \cdot 10^4$ m/s, $P_{max}/u = 10^3$ kg/s). Generally stiffer, lighter feedstock materials lead to decreased fabrication times because they decrease the mass and increase the stiffness of the fabricated structure. Figure 10 shows that for larger, denser geometries, the fabrication times are smaller for CFRP feedstock (Fig. 10(_c_)) than for both copper and steel feedstock (Figs. 10(_a_) and 10(_b_)). However, the increased specific energy consumption for CFRP extrusion results increases the importance of the power constraint and leads to increased fabrication times for smaller, coarser geometries. Comparing Fig. 10 to our analysis in Ref. [12] which solely considered the fabrication power constraint, we see that deformation processing of metals is advantageous for minimizing the fabrication time of smaller, coarser geometries, but melt-based processing of CFRP is more advantageous for

larger, denser geometries due to the decreased mass and increased natural frequencies of the resulting structures. Hence, the results in Fig. 10 suggest a truss-size-dependent tradeoff between choosing heavier feedstocks with faster fabrication speeds and stiffer, lighter feedstocks with slower fabrication speeds.

4.5 Effect of Multiple Spacecraft. Figure 11 shows the effects of increasing the number of spacecraft, $N_{SC} \in [1, 5]$, which dramatically decreases the fabrication times for the entire range of dimensions. This is due to our assumption that each spacecraft fabricates an equal fraction of the total number of struts, resulting in fabrication times that scale inversely with N_{SC} raised to a different exponent for each constraint (cf. Table 1). The greatest decrease in fabrication time with multiple spacecraft occurs for the angular momentum and flexibility constraints because each spacecraft fabricates a smaller-diameter geometry with lower mass and higher fundamental natural frequency. Figure 11 suggests that five spacecraft can fabricate 200-m diameter gridshells in five days via deformation processing of steel tubes, roughly 40 times faster than a single spacecraft with the same fabrication power and ACS authority. The results in Fig. 11 therefore suggest that
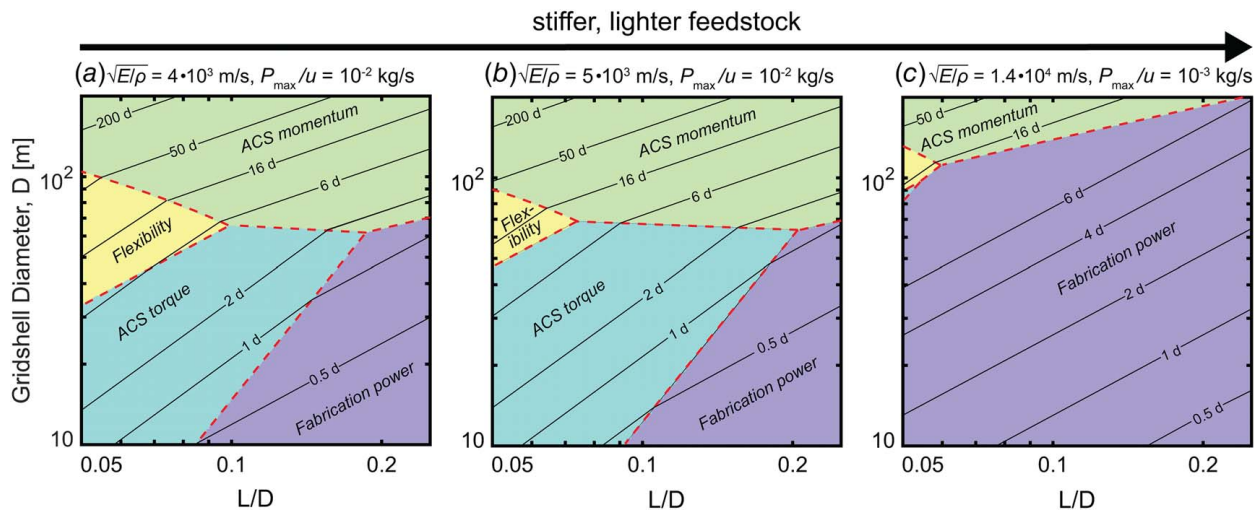

Fig. 10 Effect of feedstock material and fabrication process on the fabrication time of curved gridshells with varying diameter _D_ and strut length-to-diameter ratio _L/D_. (a) Deformation processing of copper tubes, (b) deformation processing of steel tubes, and (c) melt-based processing of CFRP tubes.
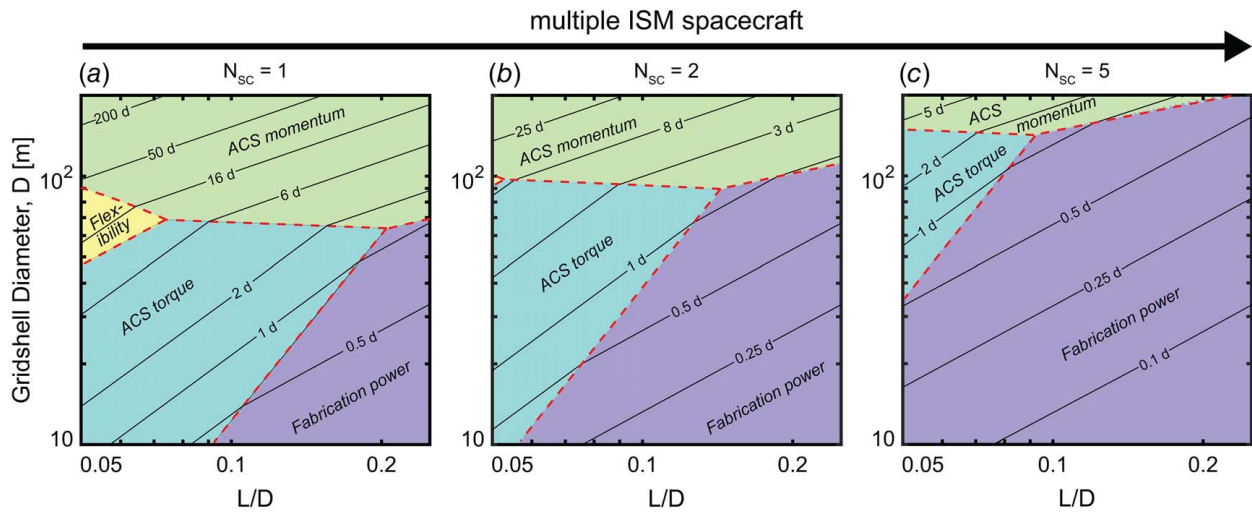
Fig. 11 Effect of multiple spacecraft on the fabrication time of curved gridshells with varying diameter *D* and strut length-to-diameter ratio *L*/*D*

multiple spacecraft are paramount for the rapid fabrication of larger, denser geometries. A caveat is that our model does not consider the assembly time of structures from each spacecraft, which may offset the benefits of using multiple spacecraft. This suggests that there is an optimal number of spacecraft for fabricating a given structure in minimum time.

4.6 Summary. As demonstrated for the curved gridshell, fabrication time diagrams are useful for visualizing and understanding the effects of the various spacecraft constraints on the total fabrication times of truss structures. The results in Figs. 7–11 show that as the gridshell diameter increases, the dominant constraints on fabrication time transition from the available fabrication power and ACS torque to the angular momentum storage and flexible body dynamics during fabrication. This transition is caused by the increased mass and decreasing fundamental natural frequencies of the structure, requiring longer extrusion times of each strut to maintain a fixed orientation and avoid control–structure interactions.

The trade studies in Figs. 7–11 suggest using multiple spacecraft, each with maximum fabrication power, maximum ACS authority, and minimal spacecraft bus mass, to minimize the fabrication time of large-diameter truss structures. These strategies increase fabrication rates, relax ACS requirements for maintaining a fixed orientation, and increase fundamental natural frequencies of the fabricated structure. For instance, our analysis suggests that five spacecraft, each with the properties listed in Table 2, can fabricate a 15-m diameter tetrahedral truss support structure for a next-generation space telescope (e.g., Large UV/Optical/Infrared Surveyor [34]) in approximately 8 h via the melt-based processing of CFRP tubes. In this way, fabrication time diagrams provide insights into the relationship between spacecraft constraints and the fabrication process, thereby guiding feedstock material selection and ACS sizing for ISM spacecraft.

5 Discussion

In this section, we discuss the implications of changing certain important assumptions in our analysis.

5.1 Extrusion of Struts Versus Assembly of Pre-fabricated Components. Our analysis focuses on ISM of truss structures via sequential extrusion of struts from raw materials such as spooled feedstock. However, our methodology is also applicable to the robotic assembly of truss structures from pre-fabricated components, known as in-space assembly (ISA). Many proposed concepts for ISA of truss structures [35–39] rely on robotic systems that assemble sub-components such as struts or deployable truss modules into support structures. For instance, a recent concept [39] envisions the robotic assembly of bays inside the spacecraft before their sequential extrusion to form a perimeter truss for a large mesh reflector antenna. For the design of such ISA spacecraft, an understanding of the relationship between the total assembly time and the spacecraft constraints is needed.

Our methodology is applicable for estimating the total assembly time for ISA concepts subject to the same constraints of fabrication power, ACS capability, and flexible body dynamics. For instance, the total power-constrained assembly time may be estimated using Table 1 with a relatively large ratio of the fabrication power to the specific energy consumption (e.g., $P_{\max}/u \approx 10^{-1}$ kg/s) to represent an efficient assembly process. Additionally, if active attitude control is required to maintain spacecraft orientation during assembly, the variable-mass rigid body dynamics model of Sec. 2.1 may be used to estimate the required ACS torque and angular momentum storage by considering the motion of the robotic manipulators. Any changes in the geometry or mass distribution within the spacecraft (e.g., from motion of pre-fabricated struts or modules) may be modeled with this framework. Furthermore, the flexible body dynamics are similarly important for robotic assembly, and as a first approximation, the fundamental natural period of the structure after each assembly step may be used to constrain the assembly time. However, additional factors should be considered for robotic assembly, including the flexible dynamics of the robotic manipulators and the structural vibrations during the attachment of joints. As a first step, the finite element modeling in Sec. 2.2 may be used to understand the vibrations from impulsive loadings during robotic assembly.

5.2 Relaxing Fixed Spacecraft Orientation Constraint. Our analysis also assumes that the spacecraft maintains a fixed orientation during the fabrication process, which constrains fabrication time due to the available ACS authority of the spacecraft. This is a strict assumption, as in reality, the spacecraft may only require intermittent attitude maneuvers to orient certain subsystems during fabrication, e.g., solar panels for recharging batteries and antennas for communication. Additionally, with omnidirectional antennas and gimbaled solar arrays [40], it is possible that the spacecraft only requires active attitude control at the end of fabrication to achieve its final desired orientation. However, estimating the total fabrication time with different attitude control strategies complicates the analysis in Sec. 2.1 and requires knowledge of specific
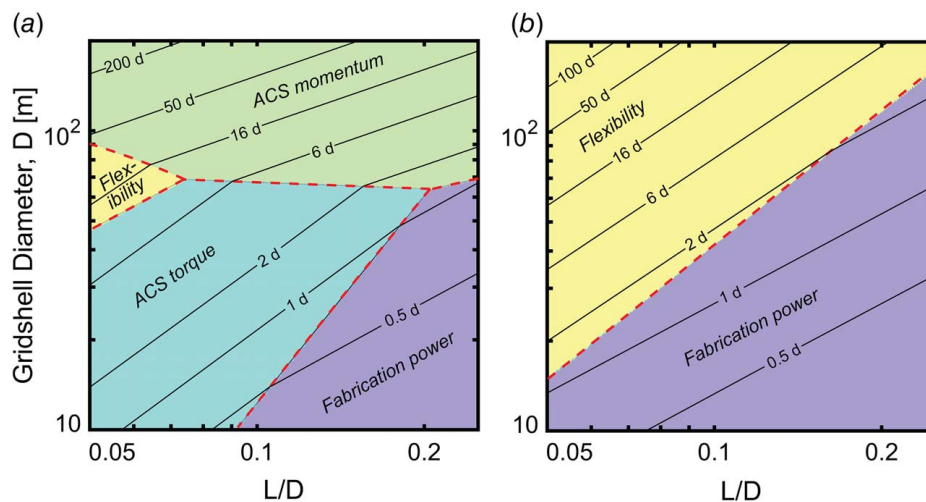
Fig. 12 Upper- and lower-bound fabrication time diagrams for curved gridshells with (*a*) fixed spacecraft orientation and (*b*) no attitude control, using the parameters of Table 2

attitude maneuvers that are difficult to generalize. Hence, to understand the effects of relaxing the fixed orientation constraint, we estimate total fabrication times with and without the ACS constraints representing the upper and lower bounds of fabrication time, as shown in Fig. 12 using the parameters of Table 2. With a fixed spacecraft orientation, larger, denser gridshells require fabrication times of over 200 days, whereas with no attitude control, the fabrication times decrease to approximately 100 days. Thus, relaxing the fixed spacecraft orientation constraint increases the fabrication rate; however, the flexible body dynamics still constrain the total fabrication times for the largest geometries. Deriving higher-fidelity fabrication time estimates requires modeling each attitude maneuver and the effects of environmental disturbances on the spacecraft during fabrication.

5.3 Varying Fabrication Paths. Another assumption in our analysis is that the structure is fabricated radially outward from its center. This results in a moment arm from the spacecraft that scales with the radius of the structure in the analytical framework, and the use of radially expanding fabrication paths in the numerical framework. As many Euler paths exist for a given truss geometry [23], this is only one approach for selecting fabrication paths. To

illustrate the effect of varying fabrication paths on total fabrication time, Fig. 13 compares fabrication time diagrams for curved gridshells with radially expanding and random fabrication paths via the numerical framework of Sec. 2.2. Here, the random fabrication paths are computed via the Hierholzer algorithm [23]. Figure 13 shows that random fabrication paths increase the importance of the flexible body dynamics and lead to increased fabrication times for denser geometries. This is because the random fabrication paths result in structures with lower natural frequencies during fabrication. This comparison illustrates that the spacecraft design is not independent of the fabrication path and highlights the potential of path optimization to minimize fabrication time.

6 Conclusions and Outlook

This paper has presented a methodology for estimating fabrication times for the ISM of truss structures accounting for various spacecraft constraints, including the available fabrication power, the ACS authority, and flexible body dynamics. Our analysis relies on the key assumptions of (1) a fabrication process that sequentially extrudes struts, (2) a fixed spacecraft orientation, and (3) negligible effects of environmental disturbance torques,
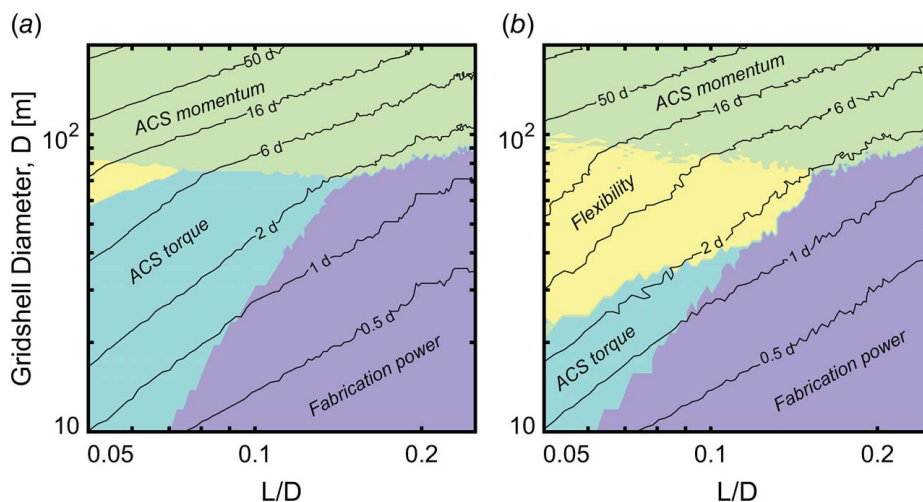

Fig. 13 Fabrication time diagrams for curved gridshells with (*a*) radially expanding fabrication paths and (*b*) random fabrication paths, using the parameters of Table 2

allowing the derivation of analytical relationships between the feedstock properties, spacecraft properties, and total fabrication time (Table 1). Some assumptions of these analytical equations, particularly regarding the geometrical approximations and flexible body dynamics, are validated with a numerical framework that models specific fabrication paths and computes natural frequencies via finite element modeling.

We have summarized our insights in fabrication time diagrams which visualize the dominant constraints and contours of fabrication time for a range of dimensions. For ISM of curved gridshell and tetrahedral truss support structures, our analysis indicates that the angular momentum storage of the spacecraft ACS is generally the most dominant constraint on fabrication time for larger geometries, whereas the available fabrication power and ACS torque generally determine the fabrication time for smaller geometries. For sufficiently large and dense geometries, however, the flexible body dynamics constraint becomes dominant due to the lower natural frequencies of the fabricated structures. Overall, our analysis suggests the following strategies for reducing fabrication times: employing multiple spacecraft, maximizing ACS authority, maximizing fabrication power, minimizing spacecraft bus mass, and using stiff and light feedstock. For example, using the parameters of Table 2, five ISM spacecraft with large reaction wheels can fabricate a 200-m diameter curved gridshell in five days via melt-based processing of CFRP tubes.

Future work is needed to refine the analysis of fabrication times in this paper. A key limitation of our model is the lack of environmental disturbance torques. For the sparse reticulated structures considered in this paper, atmospheric drag may not have a large effect; however, disturbances due to gravity gradients, magnetic fields, and solar radiation pressure should be modeled during the fabrication process. Rejecting these environmental disturbances may increase the total predicted fabrication time. Another limitation is that we do not consider the time for joint attachment, collision avoidance, and assembly of the payload on the support structure. These steps are specific to the construction process and should be included in the total fabrication time. A third area of improvement is in the modeling of fabrication time with multiple spacecraft, as the current assumption that each spacecraft fabricates an equal number of struts does not capture the complexities of collaborative fabrication. Finally, considering additional constraints on fabrication time, e.g., avoiding excessive stresses in the feedstock material, can further refine our analysis.

Overall, the methodology presented in this paper provides a starting point for the design of future ISM spacecraft and missions. The fabrication time diagrams highlight tradeoffs between the overall dimension and average facet size of support structures to achieve minimum fabrication times. These results motivate efficiently manufacturing support structures with large facet sizes and using active control methods to achieve the high precision required for payloads such as RF reflectors. Electrostatic actuation is a candidate approach for such active control via distributed actuators on coarse support structures [32]. The importance of the flexible body dynamics and ACS constraints on the fabrication time of large truss structures also motivates alternate approaches for minimizing fabrication time. For example, it may be possible to optimize the fabrication path to simultaneously maximize the stiffness of the fabricated structure while minimizing the ACS torque and angular momentum storage required for fabrication. Ultimately, distributed actuation of spacecraft structures and optimization of ISM spacecraft and fabrication processes are enabling technologies for the construction of next-generation large support structures for future space missions.

Acknowledgment

The authors acknowledge insightful discussions with Prof. Jeffrey Lang of MIT and Dr. Sonny Jeon and Dr. Mark Silver of MIT Lincoln Laboratory regarding the fabrication time diagrams.

Conflict of Interest

There are no conflicts of interest.

Data Availability Statement

The datasets generated and supporting the findings of this article are obtainable from the corresponding author upon reasonable request.

Appendix A: Variable-Mass System With Zero Angular Velocity and Acceleration

A variable-mass system is a system that loses, gains, or redistributes mass. The dynamics of such systems have been extensively studied [41–44], e.g., for understanding the rotational dynamics of rockets during flight [45–47]. In Sec. 2.1.2, the dynamics of variable-mass systems are used to model the relative motion of the spacecraft and truss structure during fabrication. Specifically, each extrusion step is modeled as a change in geometry and mass distribution within a constant mass rigid body whose orientation remains fixed with respect to inertial space. To derive the associated force and moment equilibria of Eqs. (8) and (9), we begin with the equations for a variable-mass system modeled as a control volume, reproduced from Ref. [44]:

$$\sum \mathbf{F} = \int_{CV} \rho\left(\ddot{\mathbf{R}}_0 + \dot{\boldsymbol{\omega}} \times \mathbf{r} + \boldsymbol{\omega} \times \boldsymbol{\omega} \times \mathbf{r}\right) dV$$
$$+ 2\boldsymbol{\omega} \times \left(\frac{\partial}{\partial t} \int_{CV} \rho\mathbf{r}\, dV + \int_{CS} \rho\mathbf{r}(\mathbf{w} \cdot \mathbf{n})\, dS\right)$$
$$+ \frac{\partial^2}{\partial^2 t} \int_{CV} \rho\mathbf{r}\, dV + \frac{\partial}{\partial t} \int_{CS} \rho\mathbf{r}(\mathbf{w} \cdot \mathbf{n})\, dS$$
$$+ \int_{CS} \rho\mathbf{v}(\mathbf{w} \cdot \mathbf{n})\, dS + \mathbf{F}_{\text{int}} = \mathbf{F}_{\text{ext}} \qquad (A1)$$

$$\sum \mathbf{M} = \int_{CV} \rho\mathbf{r} \times \ddot{\mathbf{R}}_0\, dV + \mathbf{J}_0 \cdot \dot{\boldsymbol{\omega}} + \boldsymbol{\omega} \times (\mathbf{J}_0 \cdot \boldsymbol{\omega})$$
$$+ \dot{\mathbf{J}}_0 \cdot \boldsymbol{\omega} + \int_{CS} \rho\mathbf{r} \times (\boldsymbol{\omega} \times \mathbf{r})(\boldsymbol{\omega} \cdot \mathbf{n})\, dS$$
$$+ \boldsymbol{\omega} \times \int_{CV} \rho\mathbf{r} \times \mathbf{v}\, dV + \frac{\partial}{\partial t} \int_{CV} \rho\mathbf{r} \times \mathbf{v}\, dV$$
$$+ \int_{CS} \rho(\mathbf{r} \times \mathbf{v})(\mathbf{w} \cdot \mathbf{n})\, dS + \mathbf{M}_{\text{int}} = \mathbf{M}_{\text{ext}} \qquad (A2)$$

Here, dot notation denotes differentiation with respect to time t, and the vectors are expressed with respect to an inertial frame: $\mathbf{R}_0$ is the position of the body-fixed frame, $\boldsymbol{\omega}$ and $\dot{\boldsymbol{\omega}}$ are the angular velocity and acceleration of the body-fixed frame with respect to the inertial frame, $\mathbf{J}_0$ is the mass moment of inertia matrix about the body-fixed frame origin, $\mathbf{r}$ and $\mathbf{v}$ are the position and velocity of a point on the body relative to the body-fixed frame, $\mathbf{w}$ is the velocity of mass leaving or entering the control volume, and $\mathbf{n}$ is the normal vector to the surface of the control volume. Equations (A1) and (A2) model the time-varying geometry and mass distribution within the control volume as forces and torques on the body, including terms for rigid body translation and rotation, Coriolis and gyroscopic coupling, and thrust from the exiting mass (see Refs. [43,44] for a complete description). If there is no time-varying geometry or mass distribution within the control volume, Eqs. (A1)

and (A2) reduce to the classical Newton–Euler equations for rigid body dynamics.

Equations (A1) and (A2) are used to compute the required ACS torque to maintain an inertially fixed orientation during strut extrusion (Fig. 2). To this end, we consider a control volume of constant mass (i.e., $\mathbf{w} = \mathbf{0}$), a body-fixed frame at the center of the mass of the spacecraft ($\mathbf{R}_0 = \mathbf{x}_{SC}$), zero external forces and torques ($\mathbf{F}_{ext} = \mathbf{0}$, $\mathbf{M}_{ext} = \mathbf{0}$), and an internal torque from the momentum actuators ($\mathbf{M}_{int} = \boldsymbol{\tau}_{ACS}$) to maintain a fixed orientation ($\boldsymbol{\omega} = \mathbf{0}$, $\dot{\boldsymbol{\omega}} = \mathbf{0}$). The terms that remain in the force and moment equilibria are

$$\sum \mathbf{F} = \int_{CV} \rho \ddot{\mathbf{x}}_{SC} \, dV + \frac{\partial^2}{\partial^2 t} \int_{CV} \rho \mathbf{r} \, dV = \mathbf{0} \tag{A3}$$

$$\sum \mathbf{M} = \int_{CV} \rho \mathbf{r} \times \ddot{\mathbf{x}}_{SC} \, dV + \frac{\partial}{\partial t} \int_{CV} \rho \mathbf{r} \times \mathbf{v} \, dV + \boldsymbol{\tau}_{ACS} = \mathbf{0} \tag{A4}$$

To compute the integrals, we model two point masses within the control volume, i.e.,

$$\sum \mathbf{F} = \sum_{i=1}^{2} m_i \ddot{\mathbf{x}}_{SC} + \frac{\partial^2}{\partial^2 t} \left(\sum_{i=1}^{2} m_i \mathbf{r}_i \right) = \mathbf{0} \tag{A5}$$

$$\sum \mathbf{M} = \sum_{i=1}^{2} m_i \mathbf{r}_i \times \ddot{\mathbf{x}}_{SC} + \frac{\partial}{\partial t} \left(\sum_{i=1}^{2} m_i \mathbf{r}_i \times \mathbf{v}_i \right) + \boldsymbol{\tau}_{ACS} = \mathbf{0} \tag{A6}$$

One point mass represents the spacecraft centered at the body-fixed frame ($m_1 = m_{SC}$, $\mathbf{r}_1 = \mathbf{0}$), and the other represents the fabricated structure at its center of mass ($m_2 = m_T$, $\mathbf{r}_2 = \mathbf{r}_T$). The total mass remains constant ($m_{SC} + m_T = M$). Substituting yields

$$\sum \mathbf{F} = M \ddot{\mathbf{x}}_{SC} + \frac{\partial^2}{\partial^2 t} (m_T \mathbf{r}_T) = \mathbf{0} \tag{A7}$$

$$\sum \mathbf{M} = m_T \mathbf{r}_T \times \ddot{\mathbf{x}}_{SC} + \frac{\partial}{\partial t} (m_T \mathbf{r}_T \times \mathbf{v}_T) + \boldsymbol{\tau}_{ACS} = \mathbf{0} \tag{A8}$$

Evaluating the time derivatives then results in Eqs. (8) and (9).

Appendix B: Effective Properties of Clamped-Free Cantilever Beam

In Sec. 2.1.3, a clamped-free cantilever beam with a tip mass and tip inertia is used to estimate the natural frequency of the truss structure connected to the spacecraft during fabrication. The effective properties of the beam are modeled as a function of the number of struts in the fabricated structure (n, N), the geometry-dependent coefficients (k, κ_0), and the strut properties (ρA, L, EI) using the following relations:

$$\overline{EI}(n) = \kappa(n) EI = \frac{\kappa_0(n - 1) - n + N}{N - 1} EI \tag{B1}$$

$$\overline{L}(n) = \frac{D(n)}{2} = \frac{L}{2} \sqrt{\frac{n}{k}} \tag{B2}$$

$$\overline{m}(n) = \frac{m_T(n)}{\overline{L}(n)} = 2\rho A \sqrt{kn} \tag{B3}$$

$$m_{tip}(n) = m_T(n) = \rho A L n \tag{B4}$$

$$I_{tip}(n) = \frac{1}{8} m_T(n) D(n)^2 = \frac{\rho A L^3 n^2}{8k} \tag{B5}$$

Appendix C: Radially Expanding Euler Paths

An Euler path is a path which traverses each edge of a graph exactly once. Here, we present an algorithm for computing radially expanding Euler paths, which "grow" from the starting node. The algorithm is based on the Fluery algorithm [23]. The radially expanding nature of the path comes from following a greedy heuristic for selecting its nodes. Specifically, all subsequent nodes of the path are chosen to be closest to the centroid of the previous nodes. The pseudocode for this algorithm is summarized in Algorithm 1. The input is a graph g with nodal coordinates pos and the output is a list of nodes that represents the radially expanding Euler path.

Algorithm 1 Radially Expanding Euler Paths

Input: truss graph (g), nodal coordinates (pos)
Output: Euler path ($epath$)
1 oddnodes = nodes in g with odd connectivity
2 **if** oddnodes empty **then**
3   firstnode ← random node in g
4 **else**
5   firstnode ← random node in oddnodes
6 **end**
7 epath ← [firstnode]
8 **while** length(epath) ≠ numedges(g) + 1 **do**
9   u = epath(end)
10   pathcoords = pos(epath)
11   centroid = mean(pathcoords)
12   allneighbors = neighbors of node u sorted by distance to centroid
13   $k = 1$
14   **while** node not added to epath **do**
15   v = allneighbors(k)
16   **if** edge (u,v) is not a bridge **then**
17   Append v to epath
18   **else**
19       $k = k + 1$
20   **end**
21   **end**
22 **end**
23 **return** epath

References

[1] Moraguez, M. T., 2021, "Modeling and Optimization of In-Space Manufacturing to Inform Technology Development," Ph.D. dissertation, Massachusetts Institute of Technology, Cambridge, MA.

[2] Lake, M. S., Peterson, L. D., and Levine, M. B., 2002, "Rationale for Defining Structural Requirements for Large Space Telescopes," J. Spacecr. Rockets, 39(5), pp. 674–681.

[3] Moraguez, M., and de Weck, O., 2020, "Benefits of In-Space Manufacturing Technology Development for Human Spaceflight," 2020 IEEE Aerospace Conference, Big Sky, MT, Mar. 7–14, IEEE, pp. 1–11.

[4] Trujillo, A. E., Moraguez, M. T., Owens, A., Wald, S. I., and De Weck, O., 2017, "Feasibility Analysis of Commercial In-Space Manufacturing Applications," AIAA SPACE and Astronautics Forum and Exposition, Orlando, FL, Sept. 12–14, p. 5360.

[5] Corporation, G. A., 1979, "Space Fabrication Demonstration System: Final Report," Technical Volume, Bethpage, NY, NASA Report N79-29213, https://ntrs.nasa.gov/api/citations/19830002888/downloads/19830002888.pdf

[6] Browning, L., and Hunt, J., 1978, "Space Construction Automated Fabrication Experiment Definition Study (SCAFEDS): Final Report, Volume II, Study Results," San Diego, CA, NASA Contractor Report 160288, https://ntrs.nasa.gov/api/citations/19790021032/downloads/19790021032.pdf

[7] Hafley, R., Taminger, K., and Bird, R., 2007, "Electron Beam Freeform Fabrication in the Space Environment," 45th AIAA Aerospace Sciences Meeting and Exhibit, Reno, NV, Jan. 8–11, p. 1154.

[8] Kugler, J., Cherston, J., Joyce, E. R., Shestople, P., and Snyder, M. P., 2017, "Applications for the Archinaut In Space Manufacturing and Assembly Capability," AIAA SPACE and Astronautics Forum and Exposition, Orlando, FL, Sept. 12–14, p. 5365.

[9] Levedahl, B., Hoyt, R. P., Silagy, T., Gorges, J., Britton, N., and Slostad, J., 2018, "Trusselator™ Technology for In-Situ Fabrication of Solar Array Support Structures," 2018 AIAA Spacecraft Structures Conference, Kissimmee, FL, Jan. 8–12, p. 2203.

[10] Kringer, M., Titz, A., Maier, P., Schill, F., Pimpi, J., Hoffman, L., Lafont, U., Reiss, P., and Pietras, M., 2024, "Effects of Microgravity and Reduced Atmospheric Pressure on Manufacturing Photopolymer Specimens," Acta Astronaut., **218**, pp. 314–325.

[11] Bhundiya, H. G., and Cordero, Z. C., 2023, "Bend-Forming: A CNC Deformation Process for Fabricating 3D Wireframe Structures," Addit. Manuf. Lett., **6**, p. 100146.

[12] Bhundiya, H. G., Royer, F., and Cordero, Z., 2022, "Engineering Framework for Assessing Materials and Processes for In-Space Manufacturing," J. Mater. Eng. Perform., **31**(8), pp. 6045–6059.

[13] Spicer, R., and Black, J., 2024, "Dynamics Simulation of a Small Satellite With a Robotic Manipulator for Additive Manufacturing," J. Spacecr. Rockets, **61**(11), pp. 1–18.

[14] Hedgepeth, J., 1981, "Critical Requirements for the Design of Large Space Structures," 2nd Conference on Large Space Platforms: Toward Permanent Manned Occupancy in Space, San Diego, CA, Feb. 2–4, p. 443.

[15] Spanos, J. T., 1989, "Control–Structure Interaction in Precision Pointing Servo Loops," J. Guid. Control Dyn., **12**(2), pp. 256–263.

[16] Marshall, M. A., and Pellegrino, S., 2023, "Slew Maneuver Constraints for Agile Flexible Spacecraft," J. Guid. Control Dyn., **46**(12), pp. 2300–2314.

[17] Miura, K., and Pellegrino, S., 2020, *Forms and Concepts for Lightweight Structures*, Cambridge University Press, Cambridge, UK.

[18] Wu, K. C., and Lake, M. S., 1994, "Natural Frequency of Uniform and Optimized Tetrahedral Truss Platforms," NASA, Washington, DC, https://ntrs.nasa.gov/citations/19950010144

[19] Eke, F. O., and Mao, T., 2002, "On the Dynamics of Variable Mass Systems," Int. J. Mech. Eng. Edu., **30**(2), pp. 123–137.

[20] Kirwan, F., 1992, *Complex Algebraic Curves*, Cambridge University Press, Cambridge, UK, pp. 203–213.

[21] Hodges, D. H., and Pierce, G. A., 2011, *Introduction to Structural Dynamics and Aeroelasticity* (2nd ed., Cambridge Aerospace Series), Cambridge University Press, Cambridge, UK.

[22] Persson, P.-O., and Strang, G., 2004, "A Simple Mesh Generator in MATLAB," SIAM Rev., **46**(2), pp. 329–345.

[23] Jungnickel, D., and Jungnickel, D., 2005, *Graphs, Networks and Algorithms*, Vol. 3, Springer, Berlin, Germany.

[24] Björck, Å., 1996, *Numerical Methods for Least Squares Problems*, SIAM, Philadelphia, PA.

[25] Marshall, M. A., 2022, "Dynamics of Ultralight Flexible Spacecraft During Slew Maneuvers," Ph.D. dissertation, California Institute of Technology, Pasadena, CA.

[26] Cardona, A., and Géradin, M., 1988, "A Beam Finite Element Non-linear Theory With Finite Rotations," Int. J. Numer. Methods Eng., **26**(11), pp. 2403–2438.

[27] Cowper, G. R., 1966, "The Shear Coefficient in Timoshenko's Beam Theory," J. Appl. Mech., **33**(2), pp. 335–340.

[28] MacNeal, R. H., 1978, "A Simple Quadrilateral Shell Element," Comput. Struct., **8**(2), pp. 175–183.

[29] Carpenter, N., Belytschko, T., and Stolarski, H., 1986, "Locking and Shear Scaling Factors in C^0 Bending Elements," Comput. Struct., **22**(1), pp. 39–52.

[30] Géradin, M., and Cardona, A., 2001, *Flexible Multibody Dynamics: A Finite Element Approach*, 1st ed., John Wiley & Sons, Chichester.

[31] Bathe, K.-J., and Wilson, E. L., 1973, "Solution Methods for Eigenvalue Problems in Structural Mechanics," Int. J. Numer. Methods Eng., **6**(2), pp. 213–226.

[32] Zhang, J. Z., Bhundiya, H. G., Overby, K. D., Royer, F., Lang, J. H., Cordero, Z. C., Moulder, W. F., Jeon, S. K., and Silver, M. J., 2024, "Electrostatically Actuated X-Band Mesh Reflector With Bend-Formed Support Structure," J. Spacecr. Rockets, pp. 1–10.

[33] Votel, R., and Sinclair, D., 2012, "Comparison of Control Moment Gyros and Reaction Wheels for Small Earth-Observing Satellites," 2012 AIAA/USU Conference on Small Satellites, North Logan, UT, Aug. 13–16.

[34] Bolcar, M. R., Aloezos, S., Bly, V. T., Collins, C., Crooke, J., Dressing, C. D., Fantano, L., et al., 2017, "The Large UV/Optical/Infrared Surveyor (LUVOIR): Decadal Mission Concept Design Update," UV/Optical/IR Space Telescopes and Instruments: Innovative Technologies and Concepts VIII, Vol. 10398, San Diego, CA, Aug. 6–10, SPIE, pp. 79–102.

[35] Lee, N., Backes, P., Burdick, J., Pellegrino, S., Fuller, C., Hogstrom, K., Kennedy, B., et al., 2016, "Architecture for In-Space Robotic Assembly of a Modular Space Telescope," J. Astron. Telescopes Instrum. Syst., **2**(4), p. 041207.

[36] Jenett, B., and Cheung, K., 2017, "BILL-E: Robotic Platform for Locomotion and Manipulation of Lightweight Space Structures," 25th AIAA/AHS Adaptive Structures Conference, Grapevine, TX, Jan. 9–13, p. 1876.

[37] Karumanchi, S., Edelberg, K., Nash, J., Bergh, C., Smith, R., Emanuel, B., Carlton, J., et al., 2018, "Payload-Centric Autonomy for In-Space Robotic Assembly of Modular Space Structures," J. Field Rob., **35**(6), pp. 1005–1021.

[38] Doggett, W., Dorsey, J., Jones, T., Mikulas, M., Teter, J., and Paddock, D., 2019, "TriTruss: A New and Novel Structural Concept Enabling Modular Space Telescopes and Space Platforms," International Astronautical Congress, Paper No. NF1676L-32522.

[39] Suh, J.-E., Thomson, S. P., Thomson, M., and Pellegrino, S., 2024, "Scalable Concept for Reflector Antenna Assembled In Space," AIAA Scitech 2024 Forum, Orlando, FL, Jan. 8–12, p. 0823.

[40] Jones, P. A., and Spence, B. R., 2011, "Spacecraft Solar Array Technology Trends," IEEE Aerosp. Electr. Syst. Mag., **26**(8), pp. 17–28.

[41] Grubin, C., 1963, "Mechanics of Variable Mass Systems," J. Franklin Inst., **276**(4), pp. 305–312.

[42] Thomson, W. T., 1966, "Equations of Motion for the Variable Mass System," AIAA J., **4**(4), pp. 766–768.

[43] Eke, F. O., 1998, "Dynamics of Variable Mass Systems," University of California Davis, Davis, CA, NASA Report 208246, https://ntrs.nasa.gov/api/citations/19980210404/downloads/19980210404.pdf

[44] Quadrelli, M. B., Cameron, J. M., and Balaram, B., 2014, "Modeling and Simulation of Flight Dynamics of Supersonic Inflatable Advanced Decelerator," AIAA/AAS Astrodynamics Specialist Conference, San Diego, CA, Aug. 4–7, p. 4454.

[45] Meirovitch, L., 1970, "General Motion of a Variable-Mass Flexible Rocket With Internal Flow," J. Spacecr. Rockets, **7**(2), pp. 186–195.

[46] Van Der Ha, J. C., and Janssens, F. L., 2005, "Jet-Damping and Misalignment Effects During Solid-Rocket-Motor Burn," J. Guid. Control Dyn., **28**(3), pp. 412–420.

[47] Eke, F., Tran, T., and Sookgaew, J., 2006, "Dynamics of a Spinning Rocket With Internal Mass Flow," Nonlinear Dyn. Syst. Theory, **6**(2), pp. 129–142.